STUDY OF' STRUCTURE AND SMALL SCALE FRAGMENTATION IN TMC1

W. D. Langer, T. Velusamy [1], T. B. H. Kuiper, S. Levin, E. Olsen

Jet Propulsion Laboratory, California Institute of Technology, MS 169-506, Pasadena, CA 91109

and

V. Migenes

Australia National Telescope Facility, CSIRO, PO Box 76, Epping, NSW 2121 Australia

---

[1] Tata Institute for Fundamental Research, Bombay, India

ABSTRACT

Large-scale $C^{18}O$ maps show that the Taurus Molecular Cloud 1 (TMC1) has numerous cores located along a ridge which extends about 12′ by at least 35'. The corm traced by $C^{18}O$ are ~ few arcmin (0.1 - 0.2 pc) in extent, typically contain about 0.5-3 $M_{\odot}$, and arc probably gravitationally bound. We present a detailed study of the small scale fragmentary structure of one of these cores, called core D, within TMC1 using very high spectral and spatial resolution maps of CCS and CS. The CCS lines are excellent tracers for investigating the density, temperature and velocity structure in dense cores. The high spectral resolution, 0.008 km s^{-1}, data consist mainly of single-dish, Nyquist-sampled maps of CCS at 2? GHz, with 45″ spatial resolution taken with NASA's 70m DSN antenna at Golds tone. The high spatial resolution spectral line maps were made with the VLA (9" resolution) at 22 GHz and with the OVRO millimeter array in CCS and CS at 93 GHz and 98 GHz, respectively, with 6" resolution. These maps are supplemented with single-dish observations of CCS and $CC^{34}S$ spectra at 33 GHz using a NASA 34m DSN antenna, CCS 93 GHz, $C^{34}S$ (2-1) and $C^{18}O$ (1-O) single dish observations made with the AT&T Bell Laboratories 7m antenna,

Our high spectral and spatial CCS and CS maps show that core D is highly fragmented. The single-dish CCS observations map out several clumps which range in size from ~45″ to 90" (0.03 to 0.06 pc). These clumps have very narrow intrinsic linewidths, 0.11 to 0.25 km s^{-1}, slightly larger than the thermal line width for CCS at 10 K, and masses about 0.03 to 0.2 $M_{\odot}$. interferometer observations of some of these clumps show that they have considerable additional internal structure, consisting of several condensations ranging in size from ~ 10" to 30" (0.007 to 0.021 pc), also with narrow linewidths. The mass of these smallest fragments can be constrained to lie in the range 0.005 to 0.05 $M_{\odot}$. The small 'scale structures traced by CCS appear to be gravitationally unbound by a large amount. Most of these objects have masses that fall below those of the putative proto-brown dwarfs ($\lesssim$ 0.1 $M_{\odot}$). The presence of many small gravitationally unbound clumps suggests that fragmentation mechanisms other than a purely Jeans gravitational instability may be important for the dynamics of these cold dense cores.

Subject headings: protostar formation - molecular cloud cores - molecules

1. Introduction

The overall structure of molecular clouds is self-similar over a range of masses which is at least 1-1000 $M_{\odot}$ (Falgarone, Phillips & Walker 1991). The observed Larson (1981) power-law relationship between the spectral linewidth and the size of clouds, $\Delta V(\mathrm{km\ s^{-1}}) \propto R(\mathrm{pc})^{0.5}$, strongly suggests that macroturbulent (supersonic) motions govern the structure of these clouds at larger scale (Miesch & Bally 1994). Under these conditions $\Delta V_{turb} \gg \Delta V_{thermal}$, where $\Delta V_{thermal} \simeq$ 0.5 to 1.0 $\mathrm{km\,s^{-1}}$ is the order of the sound speed of molecular hydrogen under typical interstellar cloud conditions. Throughout this range in ΔV, the relationship between mass, linewidth, and size is roughly consistent with the virial theorem (Myers et al. 1991; Tatematsu et al. 1993), which is to say that gravitational and pressure forces are comparable.

in the cores of cold dense clouds a different set of conditions prevails as there are many examples of linewidths measured with trace molecules, CO, CS, NH_3, HC_3N, that are narrower than the thermal linewidth of molecular hydrogen at 10 K. In these cases the velocity field is mainly thermal and has a small non-thermal component which is probably due to microturbulent (subsonic) motions, but could have contributions from systematic motion (rotation and infall). In the cores where $\Delta V_{turb} < \Delta V_{thermal}$ their support is mainly thermal pressure.

In a turbulent medium, the smallest scale in the self-similarity occurs where dissipation becomes the dominant process. Extrapolating the Larson velocity-size relationship to the point where the velocity dispersion equals the thermal linewidth of molecular hydrogen yields a scale of about 0.15 pc, or a typical size of a "Myers" core. While there is no *a priori* reason why the Larson scaling law should be valid in this regime, the results of Fuller & Myers (1993) seem to indicate that this relationship can be extended down to much narrower lines and smaller regions about 0.02-0.03 pc (4200-6200 AU). Indeed Kitamura et al. (1992) have suggested that most of the turbulent energy in the nearby quiescent Taurus Molecular Cloud-1 C (TMC-1 C) is at about this scale, 0.03 pc.

These observations of small-scale thermal features raise some important questions regarding the structure and velocity dispersion in cold cores. What are the mechanisms for fragmentation and formation of protostars? How is turbulence generated and dissipated, and how does the transition from macro- to microturbulence, and finally to purely thermal velocity dispersion take place? What decides the final state leading to, and the mass of, a protostar? What is the low-mass cutoff in for the initial mass function (IMF) and are there brown dwarfs with mass < 0.08 $M_{\odot}$? To address these issues we need extensive observations of the physical conditions in cloud cores over a large range of spatial scales.

In the classical Hoyle (1953) picture of protostar formation, hierarchical gravitational fragmentation takes place by Jeans' instability until a small enough mass is reached whereby further fragmentation halts (cf. Spitzer 1968). One problem with this model is that the fragments do not separate out in purely spherical collapse (cf. Monaghan & Lattanzio 1991). This model also dots not explain the Larson relation between size and velocity dispersion, o: the number of clumps as a function of size (cf. Williams et al. 1994) in interstellar clouds. By including outward rotation Henriksen & Turner (19S4) have proposed that the Larson relationship arises from the scaling of a compressible turbulent fluid driven by gravity and angular-momentum transfer, In contrast to such dynamical models, steady state models based on a balance between gravitational fragmentation of large clumps and coalescence of small ones (Nakano 1984) purport to explain the mass spectrum of fragments observed in large molecular cloud structures (cf. Williams et al. 1994). However it is not obvious that such models apply to the colder, less massive clouds or cloud complexes, such as the Taurus Molecular Cloud complex. Murray et al. (1993) have suggested that fragmentation by thermal instabilities and coalescence of fragments are important mechanisms in the formation of galaxies, star clusters. and individual stars. While such thermal instabilities arise readily in the diffuse ISM where different coolants in high and low density atomic gas can maintain a large contrast in temperature, it is not obvious that such states can be achieved in molecular gas where the temperature contrast is low in different gas densities.

Nearby cloud complexes afford us an excellent opportunity to study models of cloud evolution. fragmentation and protostar formation. Ground-breaking work on these cloud cores was done by Myers and his associates (e.g., Myers & Benson 1983; Benson & Myers 1989; Myers et al. 1991; Fuller & Myers 1992; Myers & Fuller 1992; Fuller & Myers 1993; Goodman et al. 1993). However to study the small scale structures within the cores we need to measure with suitable resolution the density, temperature, and velocity field of the structures in dense cloud cores. In addition, analysis of the chemical composition is important for understanding the evolution of protostellar regions. Such studies of structure and chemical composition of these cores in nearby clouds requires spatial resolution from 5″ to 45" appropriate for a wide range of scale sizes and a spectral resolution ≤ 0.03 km s^{-1}, necessary to resolve thermal widths of blended velocity components.

One of the best-studied regions of fragmentation and protostar formation is the dark cloud TMC1 in Taurus. It has been mapped at moderate resolution, 5′, in ^{13}CO, C^{18}O, and HCO$^+$ (Duvert, Cernicharo, & Baudry 1986), at $\sim 2'$ in H^{13}CO$^+$ (Guélin, Langer, & Wilson 1982), CS (Snell, Langer, & Frerking 19S2), HC$_3$N and NH$_3$ (Tone et al. 19S1) and at higher spatial resolution $\sim 45''$ in HC$_7$N (Olano et al. 19SS). All these maps show TMC1 has several moderate. size cores about 3' in diameter. Six cores were identified in the spatial-velocity CS maps (Snell et al. 1982) and CCS maps (Hirahara et al. 1992). These Myers' cores (cf. Myers et al. 1991) with size ~0.16 pc (3'-4' in diameter at the distance to TMC) have typical masses ~1 to 2 M$_\odot$ assuming an average density ~10^4 cm^{-3} as suggested by CS observations (Snell et al. 1982).

However, our understanding of the smaller-scale structures in TMC1 (cf. Hirahara et al. 1992) have been limited by the paucity of high spatial resolution observations and also the confusion that arises from the complex velocity field in this region as indicated by the line shapes of various tracers (cf. HC$_3$N spectra by Tölle et al. 19S]). Here wc extend the study of the features in TMC1 to small scale by spectral line mapping of one of its cores, called core D by Hirahara et al. (1992) and fragment-C by Snell et al. (1982) in CCS and CS down to about 6" with high spectral resolution.

The carbon chain molecule CCS is widespread in dark clouds (Fuente et al. 1990; Suzuki et al. 199'2). CCS lines are excellent tracers for investigating the velocity structure in dense cores because they have no hyperfine structure, have an intrinsically narrow thermal linewidth (0.09 km s^{-1} at 10 K), require high density for excitation and, as we show, are not very opaque in TMC1. Their intrinsic narrow thermal linewidths afford better separation of velocity structure of individual components than less massive molecules such as CO and NH_3. In addition. CCS has many accessible transitions at cm and mm frequencies that make it a good densitv probe over the range 10^4 to 10^6 cm‘³ at tile low kinetic temperatures present in dense cold cores, All these properties make CCS a potentially good tracer to search for small scale structures within the cold cloud cores.

We mapped TMC1 core D extensively in CCS at 22.3 GHz with very high velocity resolution of 0.008 km s^{-1}. Our motivation for using such high spectral resolution was that if the quiescent cloud cores were composed of many small features that it might be possible to count and separate them by resolving them spectrally rather than spatially (Velusamy et al. 1993). We also observed CCS and $CC^{34}S$ at 33.75 and 33.1 GHz, respectively, at the central position to determine whether CCS is optically thick or self-absorbed, and the CCS transition at 93 GHz to obtain excitation information about CCS. From the larger maps of CCS made with the single dish antennas we selected a few fields for observation at very high spatial resolution using interferometers: CCS 22 GHz at the VLA, CCS 93 GHz and CS 98 GHz observations at OVRO-MMA. To get an overall view of the dense regions of TMC1 we also made a large scale map of $C^{18}O$(J= 1-0) emission “ with the AT&T Bell Labs 7m antenna. our analysis of these data indicate that TMC1 is highly fragmented with structures ranging in size from 10” to 10’. The mass of the smaller clumps mapped with CCS range from about 0.01 to 0.15 $M_\odot$. The larger features traced by $C^{18}O$ range in mass from 0.5 to 30 $M_\odot$. Most of the larger structures, as seen in $C^{18}O$, are gravitationally bound while most of the smallest structures, as seen in CCS and CS are unbound. The presence of so many unbound features with masses less than those expected for proto-brown dwarfs raises important questions about their formation, lifetime and relationship) to the protostar formation process, and initial mass function.

2. Observations

The transitions observed and the telescopes used are described in ‘l’able 1. The CCS ($J_N = 2_1 - 1_0$) line rest frequency, 22,344033 GHz, is taken from Saito et al. (1987). The frequencies of the CCS and $CC^{34}S$ ($J_N = 3_2 - 2_1$) and CCS ($J_N = 8_7 - 7_6$) transitions were taken from the JPL Spectral Line Catalog (Pickett et al. 1991). Note that we have adopted the notation of Saito et al. for labeling the levels with (N,J). The JPL catalog assigns a different labeling of (N,J) whereby the N quantum number is assigned to the state of a given J which has the largest contribution from the basis function with the same N quantum number (Pickett et al. 1991). The frequency of the $J=20\rightarrow19$ transition of HC_7N was calculated from constants given by Kroto et al (1978).

Table 1: Spectral line Frequencies and Telescopes

Molecule	Transition:	Frequency (GHz)	Antenna	HPBW (arcsec)	Velocity Resolution km s^{-1}	Spatial[a] Resolution (pc)
CCS	$J=2_1\rightarrow1_0$	22.344033	Goldstone 70m	45	0.008	0.030
"	"	"	VLA -D	9	0.041	0.006
HC_7N	$J=20\rightarrow19$	22.559907	Goldstone 70m	45	0.050	0.030
CCS	$J=3_2\rightarrow2_1$	33.7.51374	Goldstone 34m	70	0.011	0.04s
$CC^{34}S$	"	33.111s39	"	"	0.011	0.04s
CCS	$J=8_7\rightarrow7_6$	93.870107	AT&T 7m	120	0.040	0.0s0
"	"	"	OVRO MMA	9	0.052	0.006
CS	$J=2\rightarrow1$	97.90968	"	6	0.049	0.00-1
$C^{34}S$	$J=2\rightarrow1$	96.412953	AT&T 7m	115	0.039	0.07s
$C^{18}O$	$J=1\rightarrow0$	109.782182	AT&T 7m	100	0.140	0.068

a. Spatial resolution calculated at the distance to TMC 1, 140 pc.

TMC1 was mapped over a 30' by 30' region in $C^{18}O$ (J=1 --O) using the AT&T Bell Laboratories 7m antenna, in 1993 and 1994. The FWHM beamwidth of the antenna is 100" at 110 GHz and our map was sampled every 60", or almost at the Nyquist sampling. The spectral resolution was 50 kHz corresponding to 0.14 km s^{-1} velocity resolution. The receiver, calibration and observing procedures are discussed in Langer et al. (1988).

We mapped one of the cores in TMC1, core-D in the CC'S map of Hirahara et al. (1992), in the CCS 22 GHz transition with high signal-to-noise, Nyquist sampling every 24" over 4' x 4' region around the peak. The map was centered at RA(19.50) $= 04^h38^m42^s.0$: DEC(1950) = 25 °34'50". The observations were made between 13 March 1993 and 1 April 1994, using NASA's 70 m-antenna (DSS- 14) at Goldstone, California. At 22 GHz the antenna HPBW is 45" and the pointing accuracy was better than 5". We measured the main beam efficiency to be 42 percent for point sources and about 70 percent for the extended source structure of TMC1, as determined from beam shape and observations of the Moon. The receiver consisted of a maser pre-amplifier followed by a digitally-controlled Hewlett-Packard down-converter with a synthesized local oscillator locked to the station hydrogen maser frequency standard. The system has a noise temperature of $\sim$60 K measured at the zenith. We used the two million channel Wide Band Spectrum Analyzer (Quirk et al. 1988) with a spectral resolution of 19 Hz over 40 MHz. The resolution was reduced by co-adding 32 adjacent channels to provide 8192 channels of 610 Hz resolution (or 0.00S km s^{-1} at 22 GHz). The spectra were observed in position switching mode and were doppler corrected to an accuracy better than 0,004 km s^{-1}.

The 33 GHz spectral line observations were made using the same spectrometer and the 34-m beam waveguide antenna of the R&D station (1) SS-13) at Goldstone with a HPBW of 70″. The receiver consisted of a cryogenically-cooled HEMT pre-amplifier followed by a two-stage down-converter which is part of the station's core equipment. The (Iow'li-converter local oscillators are locked to the hydrogen maser. The CCS 93 and $C^{34}S$ 96 GHz lines were observed with the AT&T Bell Laboratories 7m antenna in 1993-1994 using 12.5 kHz spectral resolution. The antenna half power beamwidth is 120″ and the aperture efficiency is greater than 90 percent. The receiver. calibration and observing procedures are similar to those discussed in Langer et al. (1988).

The VLA CCS spectral line maps at 22 GHz were made in D-configuration on January 4 & 6,1994 for 7 hours total, with velocity resolution $\sim$ 0.04 km s^{-1}. The data were taken using 256 channels and 0.7S MHz bandwidth without Hanning smoothing. The source 0528+ 134 was used for amplitude and phase calibration. The flux density of the calibrator was 6.14 Jy at 22 GHz. The spectral line maps were produced using AIPS. In order to maximize the signal-to-noise ratio in the maps they were smoothed to a lower resolution of 9".

The CCS and CS OVRO-MMA spectral line maps were made between October 1993 and November 1994. Our initial observations (93- 9-1 observing season) used the 5 antenna array with the map center at RA(1950) = $04^h38^m42^s.0$ and DEC(1950) = 25 °34′50″. Both the CCS and CS spectra were detected in the shortest baseline (15m) and the peak emission was observed away from the map center. In our second set of observations in October- November 1994 we used new map centers: CCS was observed at the emission peak in the VLA map; and CS was observed at emission peak seen in the earlier ( ]993-94) observations. The results presented here are from this second set of observations and used the 6 antennas in configuration A. The data were taken using 128 channels with 1.98 MHz bandwidth without on-line Hanning smoothing. Source 0528+134 was used for both amplitude and phase calibration. Tile flux density of the calibrator was 4.9 and 5.2 Jy at 93 and 98 GHz, respectively. The data were calibrated using the Owens Valley millimeter array software and the spectral line maps were produced using AIPS. In the case of the CS map the full resolution (6 ") was used. However the CCS map was smoothed to a 9″ beam in order to maximize the signal-to-noise ratio in the map.

3. Results

The $C^{18}O$ (l-O) emission traces the column density of material, except in tbe very densest cores, and gives an overall picture of the mass distribution in TMC1. Figure la shows our large scale $C^{18}O$ integrated intensity map of "l'MCl. While the $C^{18}O$ emission fills about two thirds of the map, it is brightest along a ridge roughly 12′ wide, extending along the diagonal axis about 35' (limited by the boundaries of our map). This long diagonal filament (or cylinder) contains two smaller elliptical filaments, each roughly 5' by 10' in size. The $C^{18}O$ emission also shows several cores about 2'-4' in diameter embedded in each of these elliptical features. The emission feature located near the middle of the upper border in this map is a portion of a different cloud TM - 1C (see Kitamura et al. (1993) for a full map of this region). Individual $C^{18}O$ (1-0) spectra have typical linewidths (FWHM) about 0.8 km s^{-1} and show single or sometimes blended, double peak line profiles. Figure 2 shows an example of a double peaked $C^{18}O$ profile superimposed with a CCS spectrum at the same position. The two prominent peaks in the CCS line occur at nearly the same velocities as those of the $C^{18}O$ line, but the overall velocity dispersion in CCS is considerably less than that for $C^{18}O$.

Core D occupies a small region in the $C^{18}O$ map as indicated by a rectangle in Figure 1a. Our CCS 22 GHz integrated intensity map of Core D (Figure 1b) shows smaller structures than are evident in the $C^{18}O$ map, which is consistent with the higher spatial resolution and the higher critical density for excitation of the CCS 22 GHz line. However, the location of the peaks and size of the structure seen in this CCS map cannot be taken literally because of the presence of several velocity components over most of the CCS map. Instead, as discussed below we need to use the velocity information as revealed in individual spectra,]]osit,ioll-velocity, and spatial-spatial maps at different velocities to characterize the substructure of core D.

The CCS 22 GHz spectra at all positions (observed with Nyquist sampling) are shown in Figure 3. It can be seen that these lines have very complex shapes which change significantly even among adjacent positions at the 24" sampling of the map. The signal to noise of these spectra is very high so that the changes in line shape among adjacent Nyquist sampled positions are measures of changes in density, chemical abundance, and hence structure on a scale comparable to, or less than, the beam size of 45 arcsec. The explanation for such changes that we will advocate below is that, in addition to the emission from the extended structure of core I) several, small clumps with narrow linewidths $\lesssim$ 0.15 km s^{-1} located along each line-of-sight contribute sinificantly. These clumps are likely to be embedded in larger more diffuse gas as traced by, for example, $C^{18}O$. To establish this model for the CCS line shapes we have to show that self-absorption is unimportant, that is that the dips in the spectra are not absorption features, and that the opacity is not large, Furthermore, we need to determine a characteristic linewidth of a single component in the blended line.

To check for self-absorption or shadowing we observed the map center position in CCS and $CC^{34}S$ ($J_N = 3_2$ – 21). These are plotted in Figure 4 along with CCS ($J_N = 2_1$-- 1.) and the AT&T Bell Labs CCS ($J_N = 8_7 - 7_6$) spectrum. The CCS and $CC^{34}S$ ($J_N = 3_2 - 2_1$), which have the same spatial and spectral resolution, have similar line shapes. However, the three individual velocity features are more distinct in the more optically thin $CC^{34}S$. There is no evidence in these line shapes for self-absorption: all the features seen in CCS are seen in $CC^{34}S$. '1'bus, the dips in the CCS lines are not the result of foreground absorption. Furthermore, the CCS/$CC^{34}S$ line intensity ratio is $\sim$ 12-15 across the line profile, whereas the terrestrial (and probably interstellar) value of the sulfur isotopic ratio $^{32}S/^{34}S$ is 23. Thus the 34 GHz line cannot be very optically thick and, if the excitation conditions are similar, the isotope ratio implies τ(CCS $J_N = 3_2$-2_1) <1.5 for CCS at 33 GHz. The corresponding opacity at 22 GHz can be estimated from an LVG excitation calculation (see Section 5) to be τ(CCS $J_N = 2_1$-1_0) <0.7. The HC_3N profiles of Tone et al. (resolution of 0.030 $km\,s^{-1}$) are similar to our 22 GHz CCS profile, corroborating that the optical depth effects on the 22 GHz line shape are small.

Figure 5 shows our 23 GHz HC_7N and 22 GHz CCS spectra at a position 45″ from the center. The HC_7N line is shifted in velocity with respect to the CCS line which we believe is due to the uncertainty in the calculated HC_7N frequency (see Section 2). Because HC_7N is 1.S times more massive than CCS it has an even narrower intrinsic thermal linewidth (by a factor of 25 percent) and the various overlapping velocity components separate better than in CCS. The overall width of the line at the base is about 15 percent narrower than for CCS (hyperfine splitting is negligible for this transition), which is a consequence of the narrowing of the individual outermost components that make up the line profile. Three component Gaussian fits to the HC_7N line profile yield very narrow linewidths ranging from 0.11 to 0.15 $km\,s^{-1}$ (see Table 2). We can see some indication for the presence of additional components, especially in the high velocity feature of the HC_7N spectrum which has a non-Gaussian shape.

4. Analysis

The line profiles in Figures 3 to 5 show at least three major components each with spatial structure, The CCS spectra in Figure 3 show that the emission in these three components is widely distributed along the SE-NW filament, but their intensities vary significantly from one position to the other, even at the Nyquist sampling of 24″ over almost the entire mapped region. These changes are real, rather than due to noise or baseline effects. as the signal to noise of all the spectra are very high. As noted above such changes are indicative of structural variations on a scale of the beamwidth (45″) or smaller. The variations in the line spectra from position-to-position indicate that several small features are embedded in a larger scale structure (and hence line shape) of each of these velocity components, When we fit the $CC^{34}S(J_N = 3_2 - 2_1)$ line with a combination of three Gaussians, we find (Table 2) that the peak line velocities arc 5.68, 5.S3, and 6.03 $km\,s^{-1}$ and each feature has a corresponding linewidth of 0.15, 0.12, and 0.17 $km\,s^{-1}$. The parameters for all of the lines shown in Figures 4 and 5 are given in Table 2. Though the line parameters are given to two decimal place accu racy, in many cases the errors to the velocities are even smaller, only a few meters per second. These three velocity features have different excitation temperatures as is evident from the intensity ratios among the 22, 33 and 93 GHz CCS lines, and the CCS isotope ratio at 33 GHz. The relative peak intensities of HC_7N to CCS also vary among the three main velocity components. Thus the density and CCS fractional abundances of the different main components vary.

Large Scale Spatial Structure

Disentangling the components in a map from the spectral and spatial information is a long standing and difficult problem, Various techniques have been applied in the literature including

Table 2: Results of Gaussian Fits to Line Profiles

Transition	GHz	T_A^* K	V_{lsr} [a] km s^{-1}	ΔV [a] km s^{-1}
		Component 1		
CCS	22	2.45 ± 0.03	5.70 ± 0.01	0.16 ± 0.01
Ccs	33	1.30 ± 0.53	5.72 ± 0.01	0.17 ± 0.02
CCS	93	0.674.0.03	5.70 ± 0.01	0.24 ± 0.02
$CC^{34}S$	33	0.161 ± 0.002	5.68 ± 0.01	0.15 ± 0.01
$C^{34}S$	96	0.289 ± 0.116	5.64 ± 0.02	0.203 0.03
$C^{18}O$	109	2.47 ± 0.07	5.64 ± 0.02	0.45 ± 0.04
CCS	22	2.823: 0.05	5.71 ± 0.01	0.17 ± 0.01
HC_7N	22	0.435 ± 0.016	5.52 ± 0.01	0.11 ± 0.01
		Component 2		
Ccs	22	1.75 ± 0.03	5.87 ± 0.01	0.27 ± 0.04
Ccs	33	0.07 ± 0.13	5.902 0.02	0.26 ± 0.02
Ccs	93	0.76 ± 0.07	5.96 ± 0.02	0.20 ± 0.06
$CC^{34}S$	33	0.078 ± 0.003	5.s3 3.0.01	0.12 ± 0.01
$C^{34}S$	96	0.549 ± 0.492	5.S9 ± 0.19	0.29 ± 0.27
$C^{18}O$	109	—	—	—
C c s	22	1.80 ± 0.07	5.83 ± 0.01	0.16 ± 0.01
HC_7N	22	0.491 ± 0.011	5.68 ± 0.01	0.15 ± 0.01
		Component 3		
Ccs	22	1.633: 0.14	6.0S ± 0.01	0.15 ± 0.01
C'cs	33	1.323: 0.4.5	6.0S ± 0.01	0.16 ± 0.01
Ccs	93	0.52 ± 0.26	6.0S 4:0.01	0.10 ± 0.03
$CC^{34}S$	33	0.140 ± 0.002	6.03 ± 0.01	0.17 ± 0.01
$C^{34}S$	96	0.217 ± 0.106	6.04 ± 0.09	0.20 ± 0.18
$C^{18}O$	109	1.58 ± 0.10	6.164:0.02	0.42 ± 0.05
Ccs	22	1.91 ± 0.06	6.044:0.01	0.17 ± 0.01
HC_7N	22	0.570 ±-0.013	5.S6 ± 0.01	0.14 ± 0.01

a. The values are rounded off to two decimal places; the errors in most cases are only a few m s^{-1}.

using the half-power co ntours, structure tree analysis (Houlahan & Scalo 1992), connected local minima as used in Clumpfind (Williams, de Geus & Blitz 1994), Gaussian decompositions (Stutzki & Gusten 1990), and multi-scale transforms (Langer, Anderson & Wilson 1993). 'l'here is no uniform agreement as to which (if any) is the best approach to this problem. Furthermore, they generally work best on maps with a larger data base than our CCS one. Therefore, we have decided to take a traditional approach to estimate the number of clumps by visual inspection of the peaks and contour levels in P-V and individual spatial-spatial maps for different velocity channels. The P-V map along the major (SE to NW) axis (Figure 6) has about S to 10 spatial-velocity features (clumps) within a $6'$ x 1' slice, as determined from isolating individual peaks. The angular extent of the velocity components in this P-V map ranges from 4.5" to 90" as can be seen from the size of closed contours.

Figure 7 shows the individual CCS channel spatial-spatial maps of the inner region at velocity intervals of 0.05 km s^{-1} covering the spectrum from 5.49 to 6.24 km s^{-1}. The lowest contour and the contour intervals in Figure 7 are more than six times the rms noise, and therefore the local peaks (and even the map boundaries) are statistically significant. A high degree of clumpiness in the core is evident in these maps. Visual inspection shows that there are at least eight distinct clumps which are marked a to h. The parameters for these clumps are listed in Table 3. The V_{lsr} and linewidths of the clumps were obtained by fitting a multiple gaussian to the line profile for each clump position. The CCS clump linewidths range from 0.1.5 to 0.20 km S-* . A rough estimate of size, based on closed contours around the peaks, yields a range of -1.5" to 90". The differences seen in the adjacent channel maps, which are only 0.05 km s^{-1} apart, show that there is significant blending of velocity components in the spectra. Therefore, it is likely that more features contribute to the emission in these maps but it would require higher spatial resolution. such as that possible with interferometers, to sepa.rate these.

Small Scale Structure: Interferometric Observations

Three of the clumps which wc have identified in Figure 7 appear to be less than 60" (0.04 pc) in size and are barely, if at all, resolved spatially in the 70-m beam (even though they are isolated in velocity space). To characterize these structures and to search for any smaller scale substructure we were able to make interferometric observations with the VI, A and OVRO-MMA over a limited area of the core I) single dish map. Due to the narrow line width of these structures we had to use extremely narrow channel widths of 3 and 16 kHz, respectively, for the VI, A and OVRO observations. Therefore the VLA and OVRO-MMA spectral line observations could only be made over a limited area of the core D single dish map because we were severely constrained by the observing time available to us.

In Figures 8a and 9a are shown the CCS and CS spectra obtained in the short spacings of the VI, A and OVRO-MMA (from 3000 to 8000 wavelengths in the case of the VLA and with the 15 m baseline in the case of OVRO-MMA). For comparison we also show the DSN single dish CCS spectrum at 22 GHz. All the CCS spectra correspond to the position of the clump g. The CS spectra comes from a position 20″ east of the nominal center of core D. Whereas the single dish 22 GHz spectrum has the same intensity at the 5.7 and 6.1 km s^{-1} components, in the VLA and OVRO-MMA spectra the 6.1 km s^{-1} component is distinctly stronger. Because an interferometer acts as a spatial filter its spectra contains emission from small scale structures (< 30" for the VLA and OVRO-MMA). In the case of CCS emission the small scale structures are seen prominently only in the 6.1 km s^{-1} velocity component. The 5.7 km s^{-1} component is relatively weak and does not have sufficient signal to noise to generate a spatial map. The single-dish CCS 93 GHz spectrum in Figure 4 also shows that the 6.1 km s^{-1} velocity component is more prominent. As higher densities are required for the excitation of the CCS 93 GHz transition it is likely to arise from denser and hence more compact clumps. Thus these interferometric spectra show that the 6.1 km s^{-1} velocity component contains regions of higher density and/or smaller sizes. For CS, in contrast to CCS, we only detect the 5.7 km s^{-1} component. All of the interferometer spectra have very narrow linewidths, < 0.2 km s^{-1}. Figures 8b and 9b show the high resolution spatial-spatial maps of these velocity components. The maps were made averaging the visibilities in three adjacent channels around the peaks in the spectra, that is. they are integrated over 3 channels (linewidth of about 0.15 km s^{-1}). For comparison we also show the single dish CCS maps. which trace out the larger structures, at these velocities.

The field of view of the primary beam of the VLA is 120″ and covers the central region of core D, as indicated by a box in Figure 8b. The clumps f and g (see Figure 7, particularly the panels for 6.04 and 6.09 km s^{-1}) were detected in the VLA observations (Figure 8) with intensities above the 5σ level. in the VLA map the small scale structure of clump g is extended N-S and has angular size FWHM of 20" x 30" with peak brightness of 3.0± 0.50 K. There is a suggestion of further structure in clump g in the VLA data and it may be composed of two smaller clumps, as indicated by the two intensity peaks located along the N-S axis. Clump f, located in the lower part of the VLA map, is weaker and appears to be more diffuse spatially with one bright compact region with angular size (FWHM) about 10" x 10" (0.007 pc x 0.007 pc) and peak brightness of 2.5±0.5 K. Although clumps c and e (as defined by the single-dish maps in Figure 7 at V_{lsr} = 5.69 and 5.s4 km s^{-1}, respectively) arc within the VLA primary beam no significant emission was observed at their positions and velocities,

The largest scale structures that can be observed in a full synthesis D configuration VLA map at 22 GHz is ~ 60". However, for the observations reported here, we had only partial synthesis, and therefore structures larger than 40" cannot be detected. The extremely narrow linewidth of the velocity components also severely limits the sensitivity of our observations as we had to use narrow channel widths. The absence of any detectable emission from the parts of other clumps within the primary beam of the VLA suggests that they are likely to be resolved out and have sizes larger than 40".

The OVRO-MMA field of view is about 60" at 93 GHz much smaller than that of the VLA at 22 GHz. Given the weakness of the CCS signals and the limited observing time, we restricted our OVRO-MMA observations to a field of view centered on clump g, the strongest feature in the VLA map. The 93 GHz CCS emission has been detected from clump g (Figure 9) and this high spatial resolution map shows 3 small dense embedded structures with even smaller sizes than the overall clump size in the 22 GHz VLA map. (Our OVRO-MMA maps are not sensitive to structures larger than 30'" due to the missing short spacings).; Although the overall shape of the 93 GHz CCS emission is consistent with the VLA structure of clump g the central peak is slightly displaced eastward (about 10"). The ratio of brightness temperatures of the 22 and 93 GHz CCS emission in these small scale structures is in the range of 1.5 to 2.5. The 93 GHz transition traces densities 10 to 100 times larger than the 22 GHz transition, as determined from excitation models (see below). Thus the 93 GHz CCS emission indicates the presence of high density small scale internal structure in clump g. As the sensitivity in the 93 GHz OVRO-MMA map is limited (the signal to noise ratio at the peak is only 6), wc would need higher sensitivity to investigate in more detail the density and velocity structure of clump g.

In Figure 9 we show the CS(2-1) OVRO-MMA spectrum and spatial-spatial map at V_{lsr} = 5.7 km S-l (aver-aged over a linewidth of about 0.15 km s^{-1}; see tile CS spectrum). The angular resolution of the map is 6" and the rms is 0.0S mJy/beam. The peak brightness is 1.6 K and the rms is 0.25 K. The CS clump is fully resolved and has an angular extent of about 10" x 24$''$ (0.007 x 0.016 pc) at the 3σ level. It is oriented NE-SW, that is perpendicular to the orientation of the CCS emission at this velocity (Figure 9b). 'l'he CS map shows evidence of substructure with two to three smaller clumps each $\sim$ 10" in diameter. The sensitivity in this map is not adequate for a detailed study of its velocity structure. We also note that no continuum emission at 98 GHz was detected at the 2 mJy (5u) level.

Interestingly the CS clump does not show a spatial correspondence with any of the CCS clumps in the single dish maps (see Figure 7) or VI, A maps (Figure 8), although some enhanced CCS emission is seen at the velocity and position of tile CS clump. The CS arises from a region that appears as a slight bulge, but not a distinct peak, in the CCS map. Most likely this region is a separate clump but one which cannot be clearly isolated from the surrounding emission. The lack of correspondence between the location of the CC'S and CS clumps may indicate significant chemical differentiation over small distances ((),02 to 0.04 pc). Additional evidence for chemical differentiation can be seen by comparing; the line shapes for $CC^{34}S$ and $C^{34}S$ (Figure 4).

Density Estimates

Wc can determine the excitation conditions, density, and fractional abundance of the dense clumps in core I) from the CCS and $CC^{34}S$ lines. The energy levels, frequencies, and Einstein A values for CCS were calculated using the JPL Spectral Line Catalog (Pickett et al, 1991). The 2'2, 33, and 93 GHz lines originate from levels with energies (in Kelvins) of 1.6, 3.2, and 19.9 K above the ground state, respectively. (See Figure 2 in Saito & et al. (1987) for an energy level diagram for CCS). The corresponding Einstein A values are 4.3 x 10^{-7}, 1 .6 x 10^{-6}, and 3.8 x 10^{-5} s^{-1}. We

Table 3: Parameters for Clumps Identified in Single Dish Spatial-Spatial Maps of CCS

	$\Delta\alpha$	$\Delta\delta$	T_b	V_{lsr} [a]	ΔV [a]	Size
	$''$	$''$	(K)	(km S-l)	(km s-')	($''$ x ")
a	-1oo	+30	1.58±0.61	5.63±0.01	0.18±0.02	100x6O
b	-140	+80	2.95±0.65	5.69±0.01	0.20±0.02	
c	-50	4-00	1.72±0.21	5.72±0.01	0.17±0.01	50X50
d	+00	-60	3.06±0.07	5.70±0.01	0.17±0.01	.50x50
e	+05	-40	2.153.0.05	5.87±0.01	0.16±0.01	11 OX6O
f	+10	-30	1.82±0.05	6.07±0.01	0.15±0.01	<50x.50
g	-lo	+50	1.75±0.51	6.10±0.01	0.15±0.01	75×45
h	-Go	+140	1.63±0.05	6.07±0.01	0.15±0.01	

a. The values are rounded off to two decimal places; the errors in most cases are only a few m s^{-1}.

adopt an LVG model which should be a reasonable first approximation to calculate the excitation conditions. Wc use collision rates from Fuente (1994, private communication) and Wolkovitch et al. (1995), and, unless otherwise stated, a kinetic temperature of 10 K (Fuller & Myers 1993). The 22 and 93 GHz lines have critical densities for H_2 about 10^4 and 10^6 cm^{-3}, respectively.

Presently we have multi-transition information at the central position in the single dish maps and can derive the excitation conditions only for the two clumps with size about -15" to 60" along this line of sight. We arc currently undertaking a program to map all of core D at 93 GHz with 45" angular resolution using the FCRAO antenna and will report on its density structure in a later paper (Wolkovitch et al. 1995). To derive the average density over $2'$ we first convolved the lower frequency 22 GHz data to the 120" resolution of the AT&T Bell Laboratories 93 GHz observations. We also used the 33 GHz data obtained with $70''$ angular resolution to constrain the solutions of density, $n(H_2)$, and fractional abundance, X(CCS). The brightness temperatures of the source were calculated from the antenna temperatures at 22, 33, and 93 GHz using the corresponding beam efficiencies of 70, 70, and 95 percent. For the 5.7 km s^{-1} component we find a density ~ 2 x 10^4 cm^{-3} and a CCS fractional abundance of ~ 2 x 10^{-9}. For the 6.1 km S–* component the corresponding average density is 5 x 104 cm^{-3} with a fractional abundance of 4 x 10^{-10}. These densities are consistent with those derived from CS by Snell et al. (1982) at the same resolution of 120".

On a smaller scale of 45" the 93 GHz brightness temperature is about 30 percent stronger than the Bell Labs spectra (this was determined by comparing the 7-m data to recent observations of the central position made with FCRAO's 14m antenna (Wolkovitch et al. 199,5)). Thus, at the central position of core D, we can estimate the density averaged over $45''$ from the FCRAO results in conjunction with the 22 GHz spectrum taken with the same resolution. We find a density of 3 x 10^4 cm^{-3} and a fractional abundance of 2 x 10^{-9} at 5.7 km s^{-1} and S x 10^4 cm^{-3} and 10^{-9} for the 6.1 km s^{-1} components.

For the smaller features seen in the VLA and OVRO-MMA maps ($\simeq$ 10" to 30″) we can place bounds on the density using the brightness of tile 22 and 93 GHz lines in conjunction with the LVG model. Inspection of the excitation solutions shows that the ratio of the 93 to 22 GHz brightness increases with density up to about 10^6 cm^{-3} where the lines become thermal lized. First. the density has to be greater than that estimated for the 4.5" features (> S x 10^4 cm^{-3}) as they are seen in both VLA and OVRO-MMA maps. Second, it has to be < 2 x 10^6 cm^{-3}, or else the features would be much brighter than observed in our OVRO-MMA CCS maps. Combining the interferometer line brightness with the single dish measurements provides an estimate of the total line brightness. The small scale structure in tile VLA map ($T_b \sim 3$K) is embedded in a background of about 1 1{ as seen from the single dish data. in the case of 22 GHz emission, all densities (> 10^4 cm^{-3}) along the line of sight contribute approximately equally to the total line brightness; but at 93 GHz the highest densities dominate. The differences in the u-v coverage of the VLA and OVRO-MMA maps make it difficult to estimate accurately the total line brightness at the two frequencies. Within the uncertainties in combining single dish to interferometer maps, we can place limits on the maximum and minimum total brightness in the VLA map to be about 3.5 and 6 K. Combining the OVRO-MMA and single dish observations yields a maximum brightness for 93 GHz of 2.5 K. The highest density is obtained by taking the minimum brightness for the 22 GHz line and the maximum brightness for the 93 GHz line. Thus the density and CCS fractional abundance for the minimum and maximum brightness limits are 8 x 10^4 cm^{-3} and 10^{-9} and 5 x 10^5 cm^{-3} and 5 x 10^{-11}. The most likely values are $n(H_2) \sim$ 3 x 10^5 cm^{-3} and X(CCS) $\sim$ 2 x 10^{-10}. Densities greater than 10^6 cm^{-3} are almost certainly excluded unless the kinetic temperature is about 6 to 7 K. (Our excitation analysis show that the brightness in the VLA maps are consistent with kinetic temperatures > 6 K.) We also note that there is some indication for decreasing fractional abundance of CCS with increasing densities. To derive both the kinetic temperature and density we need more data on these small fragments in another transition, preferably at 45 GHz.

Mass Estimates

We have identified several features in our $C^{18}O$ map (Figure 1 b) from local peaks and closed contours. Some of these bear a similarity to the six features identified by Snell et al. (1982) from their CS (l-O) map of TMC1. We can estimate the mass of these features using C*^{8}0 as a column density tracer of molecular hydrogen, $N(H_2)$. Assuming that $C^{18}O$ is optically thin and thermalized $N(H_2)$ is given by,

$$N(H_2) = 9.9 \times 10^{20} (1 - \exp(-5.3/T_x))^{-1} \int T_b(C^{18}O) dV \text{ cm}^{-2}$$

(Pound, Bania, and Wilson 1990) and where we use the $C^{18}O$ fractiona abundance determined by

Frerking, Langer, and Wilson (1982) for the Taurus region. The mass is obtained by integrating the column density over the projected area, A, and multiplying by the molecular weight per particle (mainly to account for Helium),

$$M(H_2) = \mu\ m(H_2) \int N(H_2)dA.$$

From the peak brightness temperature of ^{13}CO (not shown here) and our $C^{18}O$ spectra we calculate that the excitation temperature lies in the range 6-9 K. Here we adopt T_x = 7 K, the results differ by at most ± 20 percent at the limits of the range for T_x. We have applied these formula to all the features identified in the $C^{18}O$ map. In Table 4 we summarize the size and mass of the characteristic structures in TMC1. The size and mass of the entire TMC1 ridge (or cylinder) are 0.4 pc x 1.2 pc and 30 $M_\odot$. The two smaller elliptical filaments along this ridge are similar in size and have nearly identical masses, $\sim$ 10 $M_\odot$. The seven or eight $C^{18}O$ cores along TMC1 have masses in the range 0.6 to 2.5 $M_\odot$. The mass within the box around core D is 2.2 $M_\odot$. The mass we derive from $C^{18}O$ over the entire TMC1 ridge agrees very well with the value of 20-to 35 $M_\odot$ derived from CS (Snell, Langer, and Wilson 1982; Schloerb and Snell 1984).

We can use the CCS maps to estimate the mass of the smaller features embedded in core D. As noted above we do not have sufficient information to determine the density and mass of every feature within the CCS single dish and interferometer maps. However, the characteristics of the strongest clumps are similar enough to allow us to characterize the core properties from the few features where we have multi-transition information. We estimate the mass of these various clumps seen in CCS using their size and mean density.

We calculate the total mass of core 1) using the average density, 2×10^4 derived from the CCS spectra smoothed to 120", the resolution of the Bell Labs antenna at 93 GHz. This yields a total mass of 2.1 $M_\odot$ in good agreement with the mass calculated from $C^{18}O$. For the clumps just resolved in the 70-m maps with angular size $\sim 60''$ (0.04 pc), the density is $\sim 5 \times 10^4$ cm^{-3} and clump mass is $\sim$ 0.1 $M_\odot$. For the small clumps within clump *g* resolved in the VLA and OVRO-MMA maps, $\sim$ 20", the density is $\sim 3 \times 10^5$ cm^{-3} and the mass $\sim$ 0.02 $M_\odot$. For the smallest fragments just barely resolved in the VLA and OVRO-MMA maps with size $\sim$ 10" (0.007 pc) and density $\leq 10^6$ cm^{-3} their mass is likely to be very small (< 0.01 $M_\odot$).

5. Discussion

Our large scale $C^{18}O$ map shows some indication of hierarchical fragmentation in TMCl with dense cores of size 0.1 -0.2 pc embedded in larger elliptical features (0.25pc x 0.5 pc) which' are themselves part of a long filamentary, or cylindrical, structure. From the CCS single dish and interferometric maps of one of these cores, core 1), we find evidence that TMC1 probably contains many more small clumps than previously suspected. There are at least 8 clumps seen in the single dish maps of CCS with sizes about 60" (0.04 pc) at V_{lsr} between 5.6 and 6.1 km s^{-1}. At least two of these, *f* and *g*, contain small scale structure as seen in the VLA and OVRO-MMA CCS maps at 6.1 km s^{-1} and in the OVRO-MMA CS map at 5.7 km s^{-1}. There is also a hint of structure in our VLA CCS map at 5.7 km s^{-1} (see spectrum in Figure 8a) but tile signal-to-noise is not good enough for this velocity component to produce a reliable, high resolution map. At least one of these clumps is composed of, or contains, 3 to 6 smaller scale components with sizes about 0.01 pc as seen in both our VLA and OVRO-MMA maps. These small scale structures in the interferometer maps may represent high density condensations or fragments within the clumps. Our best estimate of the density of these small fragments is 11(112) about 3 x 10^5 cm^{-3} and CCS fractional abundance about 2 X 10^{-10}.

Table 4: Parameters of the characteristic sub-structure in TMC

Structure	Tracer	Size pc	11(112) 10^4 cm^{-3}	Mass $M_\odot$	Virial Mass[a] $M_\odot$	Comments
TMC1	$C^{18}O$	1.2 x 0.4	--	30	52	bound
SE-filament	C'so	0.6 X 0.25		10	29	bound
cores	C'so	0.1 -0.2		[).5 -3.2	5 - 15	bound
core D	Ccs	0.1s x 0.12	2	2.0	3.6	bound
clumps	Ccs	0.04	5	0.1	0.96	unbound?
small fragments	Ccs	0.01	30	0.01	0.24	unbound-transient

a. using ΔV= 0.S5 and 0.48 km s^{-1} respectively for $C^{18}O$ and CCS tracer

The CCS linewidths are very narrow (both in the single dish and interferometric spectra) and are composed of a thermal and nonthermal component. The velocity dispersion due to turbulent motions, σ_{turb}, within the clumps can be obtained from the CCS linewidths by

$$\sigma_{turb} = \sqrt{\sigma_{tot}^2 - \sigma_{therm}^2}$$

where the total dispersion, σ_{tot}, is related to the line full width at half maximum, $\Delta V = 2.35\sigma_{tot}$ The velocity dispersion due to thermal motions is

$$\sigma_{therm} = 0.0912 \sqrt{\frac{T}{m_{AMU}}} \text{ (km s-l)},$$

where m_{AMU} is the molecular mass give in AMU. For CCS at 10 K the thermal velocity dispersion is 0.0386 km s–'. A value of $\Delta V < 0.15$ km s^{-1} implies a turbulent velocity dispersion less than 0.05 km s^{-1}, which is smaller than the sound speed (0.19 km s-') in a gas with mean molecular weight of 2.3 amu. Thus the thermal pressure due to molecular hydrogen at 10 K (corresponding to a ΔV = 0.4S km s^{-1}) is much greater than the turbulent pressure even in the larger fragments. From a comparison of the HC_7N and CCS linewidths in Table 2, we estimate σ_{turb} to be < 0.06 km s-1. Thus thermal pressure (due to molecular hydrogen) is dominant in the core and the clumps, and turbulence is not a significant factor in their support.

1)0 these fragments display any relationship between size and velocity dispersion? It is claimed for dark clouds (cf. Figure 12 of Tatematsu et al 1993) that the linewidths appear to obey the empirical relationship $\Delta V \propto (\Delta R)^{0.5}$ down to the thermal linewidth. For the clumps in Table 3, we find no evidence of such apparent scaling. However as pointed out above, there is large degree of blending in both spatial and velocity domains, and the clump sizes and the velocity widths are probably overestimated in Table 3.

Table 4 lists masses derived from $C^{18}O$ column densities and densities estimated from CCS line intensities for different (larger to smaller) scale size structures observed in TMC1. We can draw some conclusions about the stability of these structures by comparing these masses with the corresponding virial mass M_{vir}. The virial masses listed in Table 4 were estimated using the relation $M_{vir} = 210\ R\ (\Delta V)^2$, taken from MacLaren et al. (1988) for constant density distribution. For the large scale structures traced by $C^{18}O$ we used $\Delta V = 0.85$ km s-1, the mean width of the $C^{18}O$ profile (Figure 2). In the case of the small scale structures traced by CCS, as described above, turbulence is negligible and we have to consider only the thermal pressure of H_2. Therefore, for AV we used the thermal linewidth for an H_2 molecule at 10 K. The virial masses estimated assuming constant density are not very different (less by 15 percent) for a l/r density distribution. If a structure has mass, $M > \frac{1}{2}M_{vir}$ it is bound, and if $M \geq M_{vir}$ will be unstable to collapse. The structures with $M < \frac{1}{2}M_{vir}$ are unbound. However when applying the above criteria one must be aware of the rather high uncertainties in the mass estimates (within a factor ~ 2 from $C^{18}O$ and, factors of about 2 and 10 from CCS observations for the 60" and 10" structure; respectively). The properties of the different features indicated in Table 4 represents the most likely structure suggested by our observations.

Overall, core D appears to be bound, but is not likely to be unstable against collapse. However, the smaller structures within this core are unbound. The clumps which are barely resolved in the single dish maps ($\sim$ 60") appear to be unbound, or at most a few may be marginally bound. Those clumps resolved in the interferometers with sizes < 20" have a virial mass much greater than their actual mass. Hence it appears that the features traced by CCS from 10" to 30" are most likely unbound and subject to expansion unless they are pressure confined. The presence of such unbound clumps within a cloud core suggests that fragmentation mechanisms other than a purely Jeans' gravitational instability may be important in cold dense cores.

As the mass estimated from the density for the smaller fragments is an order of magnitude less than the virial mass and they cannot be bound unless they have higher densities $\sim 10^7$ cm^{-3}.

Although such high density is not evident in the data presented here, it cannot ruled out if the kinetic temperature is much lower than 10 K, about 6 or 7 K.

It has been suggested, on the basis of the NH_3 abundance, that the south-eastern part of TMC1 filament (which includes core-~) contains the youngest cores (Tölle et al. 1981; Olano et al. 1988; Hirahara et al. 1992). Thus the clumpiness observed with CCS may describe the physical and chemical condition of the gas at very early stages of clump formation and evolution. The single dish CCS maps show that the fragments are distributed along the filament and that they have a very narrow width perpendicular to the filament. Our high resolution OVRO-MMA and VLA maps resolve the structure perpendicular to the filament at some places into small scale structures. Carbon chain molecules (CCS and cyanopolyynes) may be produced most efficiently in small fragments with enhanced densities. The density enhancements seen along the SE-NW filamentary-l like structure may arise from fragments formed in a compressed region produced by cloud collision (Little et al. 1978) or contraction along the predominant magnetic field (Moneti et al. 1984). Quasi-periodic structure (as seen on a larger scale in Figure 1a and on a smaller scale in Figure 6) could be due to some magnetohydrodynamic mode (Langer 1978; Carlberg and Pudritz 1991). The distribution of CCS and CS clumps in Figures 1, 7, 8 and 9 suggests that one of these mechanisms is present, especially given their low mass. As noted above, the turbulent velocity dispersion is small ($\leq$ 0.0.5 km S-1) compared to the thermal velocity dispersion of a 10 K gas with mean molecular mass of 2.3 amu. We have searched for velocity gradients in our data and find that the rotation is small, $\lesssim$ 0.0.5 km s-1 arcmin^{-1} (1.25 km s-1 pc^{-1}), and makes negligible contribution to support.

What are these clumps in TMC1 core D? Do they represent localized regions of density or chemical inhomogeneities or both? As the mass estimated for the smaller clumps with a density $\sim 10^5$ to 10^6 cm^{-3}, is much less than the virial mass these clumps are not gravitationally bound. Because TMC1 appears to be unusual in chemistry and structure, it might secm that conclusions about this source cannot be applied to low-mass star forming regions in general. However, the properties of the clumps in TMC1 core D are similar to the properties of the quiescent core in L1498 (Lemme et al. 1995; Velusamy et al. 1995). Lemme et al. found from high resolution $C^{18}O$ and CS observations that 1,1498 consists of a large bound core with very narrow linewidths, 0.11-0.18 km s^{-1}, with mass $\sim 1\ M_{\odot}$. This core is in virial equilibrium and is thermally supported. Their $C^{18}O$ (2-1) data also showed many small sub-solar mass, gravitationally unbound clumps, with narrow line features, similar to the features we extract from our CCS maps of TMC1. Interferometer observations in CS also show the presence of < 0.01 pc small scale structures in L1498 core (Velusamy et al. 1995). The presence of such structures in both clouds raises some interesting questions about their formation. The more complex structure of TMC1 may be a collection of objects similar to the L1498 core.

From the number of features in the maps using different density tracers and at different spatial resolution there appears to be a hierarchy of fragments with an increasing number of features at smaller scales embedded in the larger scale features. While our maps are limited to core D it appears that the number of features continues to increase at smaller scales, at least down to 0.007 pc. Indeed we see more smalls scale features per unit area than do Pound and Blitz (1995) who used different tracers to search for low mass objects in star forming regions Oph B and B18. However, we find no evidence for proto-brown dwarfs (bound structures with mass < 0.0S $M_\odot$) similar to the conclusions of Pound and Blitz (1993, 1995). We need more observations to say whether the number distribution turns over at very low mass (< 0.1 $M_\odot$).

We believe that the small sub-solar mass objects seen in TMC1 core D are an important part of the protostar formation process because of the possibility of coalescence. It has been suggested that fragmentation by thermal instabilities and coalescence of small fragments arc important in the formation of stars in the interstellar medium (Murray et al. 1993). Silk (199.5) suggests that low mass fragments grow by coalescence (through collisions) and are likely to form stars with low mass $\sim$ 0.2 or 0.3 $M_\odot$. The time scales for dissipation of our CCS fragments (size/sound speed) is $\sim 10^5$ yr for a 20" feature. Most of the small scale fragments ($\leq$ 40") will dissipate because the sound crossing time is somewhat less than the collision time of a few $\times 10^5$ yr (depending on the size and assumed velocity dispersion *among* the fragments). However a fraction of these fragments will collide and perhaps coalesce to form denser bound structures. Because many of the fragments with size 20" to 45″ are within a factor of 2 - 3 of having sufficient mass to be bound it would not take more than one or two coalescing collisions to form a bound structure. On the other hand the smallest features detected in our maps, size $\sim$ 10", are so far from being bound (in terms of gravitational mass) that they almost certainly dissipate before colliding with other similar fragments unless they are pressure bound. The sound speed of ~ 0.2 km s^{-1} for these features suggest that they are transient with lifetimes < ,5 x 10^4 yr and that if, they are long lived they must be pressure confined.

It is possible that the small clumps fragments are confined by turbulent pressure, since they are embedded (along the axis of the filament) in a more turbulent (velocity width $\sim$1 km s^{-1}) lower density gas as traced by $C^{18}O$ (Figure 2) and ^{13}CO and, perhaps with some additional magnetic contribution as well (eg: Bertoldi & McKee, 1992). Thus they could have longer lifetimes than estimated here and may have more time to coalesce.

The low masses of the fragments raise another interesting question, -' do *they represent a* population of proto-brown dwarfs? Pound and Blitz (1995) claim to see a cutoff in the number of bound clump masses below 0.1 $M_\odot$ in the star forming regions Ophiuchus and B18. Although we find that low mass clumps are more prevalent in a quiescent region than Pound and Blitz, they are all unbound and hence would not form a proto-brown dwarf without some collisional process.

6. Summary

We have made a study of the structure of TMC1 and, in particular, of Core D on scales ranging from 10" up to 30' using single dish and interferometric maps of $C^{18}O$, CCS, and CS.

Our $C^{18}O$ map shows hierarchical fragmentation with dense cores embedded in larger elliptical features which are part of a long filamentary, or cylindrical. structure. From the CCS single dish and inter ferometric maps we find evidence for many more small scale structures in individual cores in TMC1 than previously suspected. The high spectral and spatial CCS maps of TMC1 show that core 1) is highly fragmented with structures ranging in size from 10 to 90 arcsec. These small fragments have very narrow intrinsic linewidths $\leq$ 0.11-0.20 km S–1 , not much larger than the thermal line width for C('S (0.09 km s^{-1} at 10 K). These narrow linewidths indicate that H_2 thermal pressure is the dominant support in these clumps and that turbulence and rotation are not significant. The mass of these fragments range from $\lesssim$ 0.01 to 0.15 $M_\odot$ as estimated from density and volume. '

The structure of TMC1 can redescribed as hierarchical from large to extremely small scale sizes roughly over two orders of magnitude consisting of: (i) long filaments of size > 0..5 pc and mass of several $M_\odot$; (ii) several cores (which are gravitationally bound) of size $\sim$ 0.1 pc and masses 0.5 to 3 $M_\odot$ distributed along the filament; (iii) each core contains several clumps of size $\sim$ 0.04 pc and mass $\sim$ 0.1 $M_\odot$ which are mainly gravitationally unbound; and, (iv) some of these clumps themselves contain smaller fragments of size $\sim$ 0.01 pc and mass $\sim$ 0.01 $M_\odot$ which are almost certainly unbound. The small scale structures appear to be gravitationally unbound which suggests that fragmentation mechanisms other than a purely Jeans gravitational instability may be important in cold dense cores, or that external pressure confinement is important.

We thank the DSN Goldstone staff for help in operating the 70m and 34m antennas and the WBSA, the staffs of the NRAO VLA and the OVRO-MMA for assistance in the interferometer observations, Drs. G. Wright and R. W. Wilson helped with the $C^{18}O$ map. Dr. A. Fuente and D. Wolkovitch kindly provided information on CCS collision rates, and Dr. H. Pickett advised us regarding the atomic and line properties of CCS. Drs. S. Gulkis and M. Klein have encouraged and supported our work with the DSN antennas. This research was conducted while T.V. held a National Research Council - Senior Research Associateship while on leave from the Tata Institute. This research was performed at the Jet Propulsion Laboratory, California Institute of Technology, under contract with the National Aeronautics and Space Administration. The VLA of the National Radio Astronomy Observatory is operated by Associated Universities Inc., under contract with NSF. The OVRO millimeter array is supported by NSF grant AST 90-16404.

REFERENCES

Bertoldi, F, & McKee, C.F. 1992, ApJ, 395, 140

Carlberg R.G. & Pudritz R. E. 1991, MNRAS, 247, 353

Duvert, G., Cernicharo, J. & Baudry, A. 1986, A&A, 164, 349

Falgarone, E., Phillips, T. G. Walker, C. K. 1991, ApJ, 378, 186

Falgarone, E., Puget, J.L. & Pérault, M. 1992, A&A, 257, 715

Fiebig, D. 1990, Doktorarbeit, Univ. Bonn

Frerking, M. A., Langer, W. D., and Wilson, R. W. 1982, ApJ, 262, 590

Fuente, A., Cernicharo, J., Barcia, A. & Gómez-González J. 1990, A&A, 231, 151

Fuller, G. A. & Myers, P. C. 1992, ApJ, 384, 523.

Fuller, G.A, & Myers, P.C. 1993, ApJ, 41S, 213

Goldsmith, P.F. & Langer, W.D. 1978, ApJ, 222, SS1

Goodman. A. A., Benson, P. J., Fuller, G. A. & Myers, F'. C. 1993, ApJ, 406, 528.

Guélin, M. & Cernicharo, J. 1988, in *Molecular Clouds in the Milky Way and External Galaxies*. ed. R. 1.. Dickman, R. L. Snell and J. S. Young (Berlin: Springer-Verlag), S1.

Herbst, E. & Leung, C.M. 1986, MNRAS 222, 689

Hirahara, Y., Suzuki, H., Yamamoto, S.. Kawaguchi, K.. Kaifu, N., Ohishi, M., Takano, S.. Ishikawa, S. & Masuda, A. 1992, ApJ, 394, 539

Houlahan, P. & Scale, J. 1990, ApJ, 393.172

Hoyle, F. 1953, ApJ, 118, 513

Kitamura, Y., Sunada. K., Hayashi, M. & Hasegawa, T. 1993, ApJ, 413, 2'21.

Kroto, 11., Kirby, C., Walton, 1). R. M., Avery. 1,. W., Broten, N. W., MacLeod, J. hi., & Oka, T. 1978, ApJ, 219, L133

Langer, W.]). 197S, ApJ, 225, 95

Langer, W.])., Wilson, R.W. & Anderson, C.H. 1993, ApJ, 40S, 1,45

Lemme, C., Walmsley, C. M., Wilson, T. L., and Muders, D. 1994, A&A, in press

Little, L. T., Macdonald, G.II., Riley, P.W. & Matheson, D.N. 1978, MNRAS, 183, 805

MacLaren, 1., Richardson, K, M., & Wolfendale, A. IV. 1988, ApJ, 333, 821

Miesch, M. S. & Bally, J. 1994, ApJ, 429, 645.

Monaghan, J. J. & Lattanzio, J. C. 1991, ApJ, 375, 177

Moneti, A., Pipher, J.]., Helfe, 11.1,., McMillan, R. S., & Perry, M.L. 1984, ApJ, 2S2, 508

Mι ırray, S. 1)., White, S. D.M., Blondin, J. hi., and Lin, D.N.C.1993, ApJ, 407, 588

Myers, P.C. & Benson, P. J. 1983, ApJ .266, 309.

Myers, P. C., Fuller, G.A., Goodman, A. A. & Benson, P. J.1991, ApJ, 376, 561.

Nakano, 'I'. 1984, Fund. Cosmic Phys., 9, 139.

Olano, C.A., Walmsley, C.M. & Wilson, '1'.1,. 1988, A&A, 196.194

Pickett, H. H., Poynter, R. and Cohen, E. 1991, Submillimeter, Millimeter and Microwave Line Catalog 3e, JPL Tech. Rep. SO-23

Pound, M.W., Bania, T. M., and Wilson, R. W. 1992, ApJ, 351, 165

Pound, M.W. & Blitz, L. 1993, ApJ, 418, 328

Pound, M. W. & Blitz, L. 1995, ApJ, in press

Quirk, M. 1'., Wilk, M.F., Garyantes, M. F. & Grimm , M.J. 19SS, IEEE Trans. on Acoustics. Speech & Signal Processing 36, 1S54

Saito, S., Kawaguchi, K., Yamamoto, S., Ohishi hi., Suzuki. 11. & Kaifu, N. 1987, ApJ, 317, L115.

Silk, J. 1995, ApJ, 43S, L41

Schloerb, F.P. & Snell, R.L. 1984, ApJ, 2S3, 129

Snell, R.]., Langer, W.D. & Frerking, M.A. 19S2, ApJ, 255, 149

Stutzki, J. & Gusten, R. 1990, ApJ, 356, 513

Suzuki, H., Yamamoto, S., Ohishi, hi., Kaifu, N., Ishikawa, S., Hirahara, Y., Takano, S. & Masuda, A. 1992, ApJ, 392, 5.51.

Tatematsu, K., et al. 1993, ApJ, 404, 643.

Tone, F., Ungerechts, H., Walmsley, C.M., Winnewisser, G. & Churchwell, E. 19S1, A&A, 9.5, 143.

Velusamy, T., Kuiper, T. B.H., Langer, W.D., Levin, S., Olsen, E.T. 1993 in Proc. 2nd Zermatt Conf. *The Physics and Chemistry of Molecular Clouds*

Velusamy, T., Kuiper, T.B.H., Langer, W.D. 1995 (in preparation)

Williams, J.P., de Geus, E., & Blitz, L. 1994, A&A, 428, 693.

Wolkovitch, D., Goldsmith, P. }'., Langer, W. 1)., Kuiper, '1. B. 11., Heyer, M., Velusamy, T., and Levin, S. 1995, private communication.

Zinnecker, H. 1989, in *Evolutionary Phenomena in Galaxies*, ed. J. Beckman (Cambridge University Press) p115.

This preprint was prepared with the AAS LaTeX macros v3.0.

Fig. 1--- (a) $C^{18}O$ (1-0) integrated intensity map of TMC1 from the AT&T Bell Labs 7m antenna: 1' sampling; 1.7' beam size. The lowest contour and the contour interval are 0.4 and 0.2 K km s^{-1}, respectively. The box represents the region containing core D centered at 1{.4(1950) = $04^h38^m42^s.0$; DEC(1950) = 25 °34'50";
(b) CCS 22 GHz total integrated intensity map of Core I) over a $4'$ by $4'$ region, These data arc taken with the DSN 70-m antenna which has an ang ular resolution of 4.5"; the map is Nyquist sampled every 24". The first, contour and contour interval are 0.075 K km S-l. The circles at the top left corners represent the respective antenna beam size.

Fig. 2.- $C^{18}O$ and CCS spectra at the central position in TMC1 core D. The $C^{18}O$ and CCS velocity channel widths are 0.14 and 0.00S km S-*, respectively. The CCS spectrum was smoothed spatially to a lower resolution of 100" corresponding to the angular resolution of the Bell Labs 7-m antenna.

Fig. 3.- Plotted are all the CCS spectra at 22 GIIz in core D taken with the 70-m antenna. The spectra were observed every 24" in both north-south and east-west directions; the antenna beamwidth is 45". The channel width is 0.00S km s^{-1} and the spectra are smoothed to a velocity resolution of 0.025 km S--l.

Fig. 4--- High spectral resolution lines in TMC1 core D at the position RA(1950) = $04^h38^m42^s.0$; DEC(1950) = 25 °34'50". The 22 and 33 GHz profiles are sampled every 0.008 and 0.011 km s^{-1} respectively and are smoothed to 0.02.5 and 0.04 km s^{-1}. The CCS 93 and $C^{34}S$ 96 GHz profiles have spectral resolutions of 0.04 km s-', and were taken with the 7-m antenna (beam resolution 120").

Fig. 5--- High spectral resolution lines of CCS and HC_7N in TMC1 core D at the position RA(1950) = $04^h38^m44^s.3$; DEC(1950) = 25 °34'14". The 22 GHz profiles are sampled every 0.008 km s^{-1} and arc smoothed to 0.025 km s^{-1}. The HC_7N lines show three distinct components and the central and high velocity features are probably composed of two blended velocity components. The HC_7N frequencies were calculated from the molecular constants and the shift in velocity with respect to CCS is due to the uncertainties in the frequencies. We did not correct the HC_7N frequencies to line up with those of CCS.

Fig. 6.—- CCS position-velocity map of core D along the SE to NW direction approximately passing through the three peaks in Figure lb. Velocity and angular resolutions are 0.025 km s^{-1} and 45" respectively, but sampled at 0.008 km s^{-1} and 24". The first contour and interval are 0.15 K and the rms = 0.04 K. There are eight separate features along this cut with sizes about 45" to 90".

Fig. 7.-. Goldstone 70-m CCS intensity spatial-spatial maps of TMC1 core D, one map is shown for every 0.05 km s^{-1} velocity interval. 'l'he contours are integrals over 0.05 km s-l, and the lowest contour and contour interval are 0.2 K km s^{-1}. Each map is centered at RA(1950) = $04^h38^m42^s.0$; DEC(1950) = 25 °34'50". 'The eight clumps we identify in the CCS data cube are labeled *a* to *h*. The circle at the top left corner represents the beam size.

Fig. s.- a) The spectra for CCS at 22 GHz from the DSN and VLA and the CCS 93 GHz OVRO spectra at the position of clump *g* (see Figure 7) arc displayed. The VLA spectrum is that for the shortest baseline (3000 to S000 λ). The OVRO spectra were observed in the 15 m baseline. The peak at 6.1 km s^{-1} is clearly resolved at both 22 and 93 GHz. There is evidence for a second velocity component at 5.7 km S-l in both spectra. The arrows indicate the velocity (channel) of the maps shown in (b).
b) VI. A CCS 22 GHz and OVRO CCS 93 GHz spatial maps for the velocity component 6.00 km s^{-1}. The single dish 70 m CCS (22 GHz) map is shown at the top for comparison. The mapped regions are indicated by boxes. The center of the 70 m map is at the nominal center of Core-1) as shown in Figure 7. The spatial resolutions in the VLA and OVRO maps are $9'' \times 9''$. The first contour level and interval in the VLA map are 16 mJy beam^{-1}(0.50 K in T_b); the rms noise in the map is 14 mJy beam--]. The first contour level and interval in the OVRO map are 120 mJy beam^{-1} (0.20 K in T_b); the rms noise in the map is 90 mJy beam- ^{1}. The VLA map shows a strong condensation at the position of clump *g* which may have two subclumps. The OVRO 93 GHz map of this region traces out several high density clumps. 'l'he circle at the top left corner of the maps represents the beam size.

Fig. 9.— a) The CS (2-1) spectrum observed with OVRO shows prominent emission at 5.7 km s^{-1}. The corresponding single dish CCS 22 GHz spectrum is also shown for comparison. The arrows indicate the velocity (channel) of the maps shown in (b).
b) OVRO CS (2-1) map at V_{lsr} = 5.7 km s-1. The single dish 70 m CCS 22 GHz map at this velocity is shown at top. The OVRO map region is indicated by a box, The center of 70 m map is at the nominal center of core D as shown in Figure 7. The spatial resolution in the OVRO maps is $6'' \times 6''$. The lowest contour level and contour interval are 100 mJy beam^{-1} (0.35 K in T_b); the rms noise in the map is 85 mJy beam^{-1}. The CS is concentrated in 3 or 4 small clumps located along a ridge running NE-SW. The CS feature is located at a position in the single dish CCS map (top panel) that appears as a bulge. This position probably marks a separate 45" clump that is blended in this map. The circle at the top left corner of the maps represents the beam size.

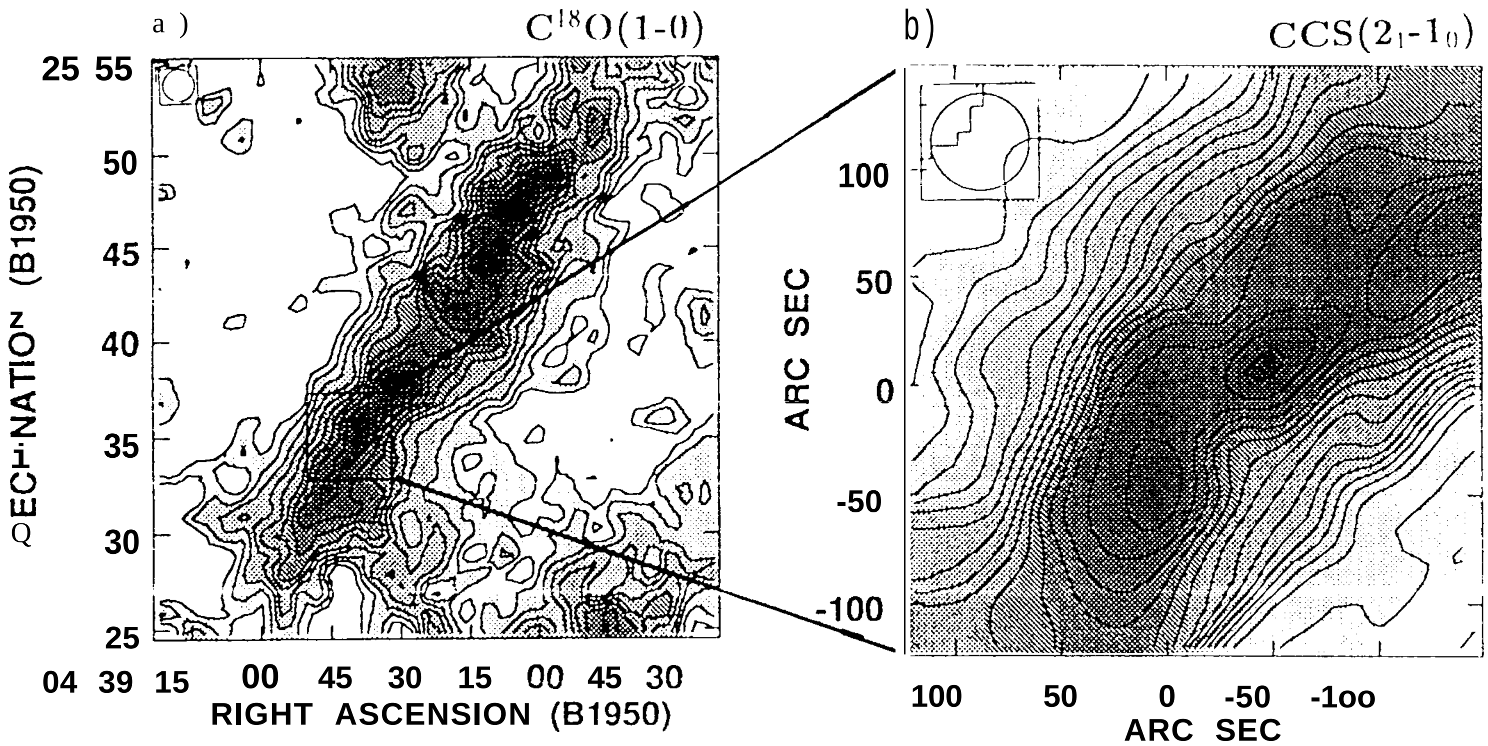

a)
C18O(1-0)
25 55
50
45
40
35
30
25
DECLINATION (B1950)
04 39 15 00 45 30 15 00 45 30
RIGHT ASCENSION (B1950)
b)
CCS(21-10)
100
50
0
-50
-100
ARC SEC
100 50 0 -50 -100
ARC SEC

Fig. 1

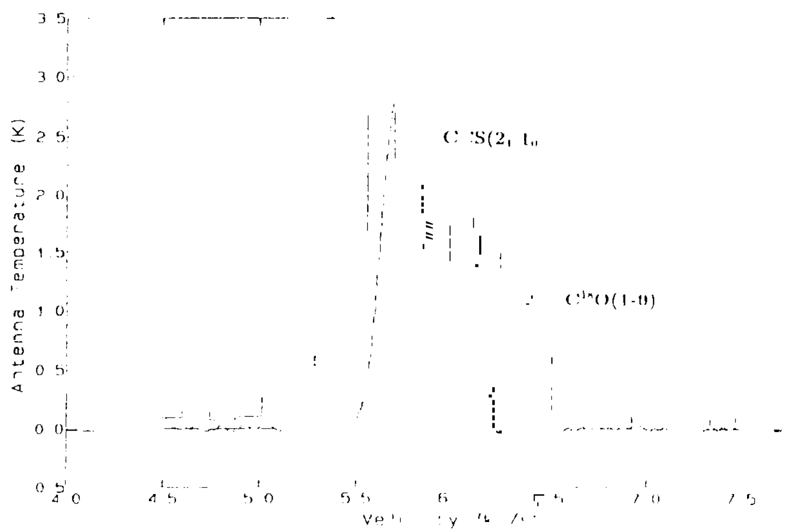

Fig 2

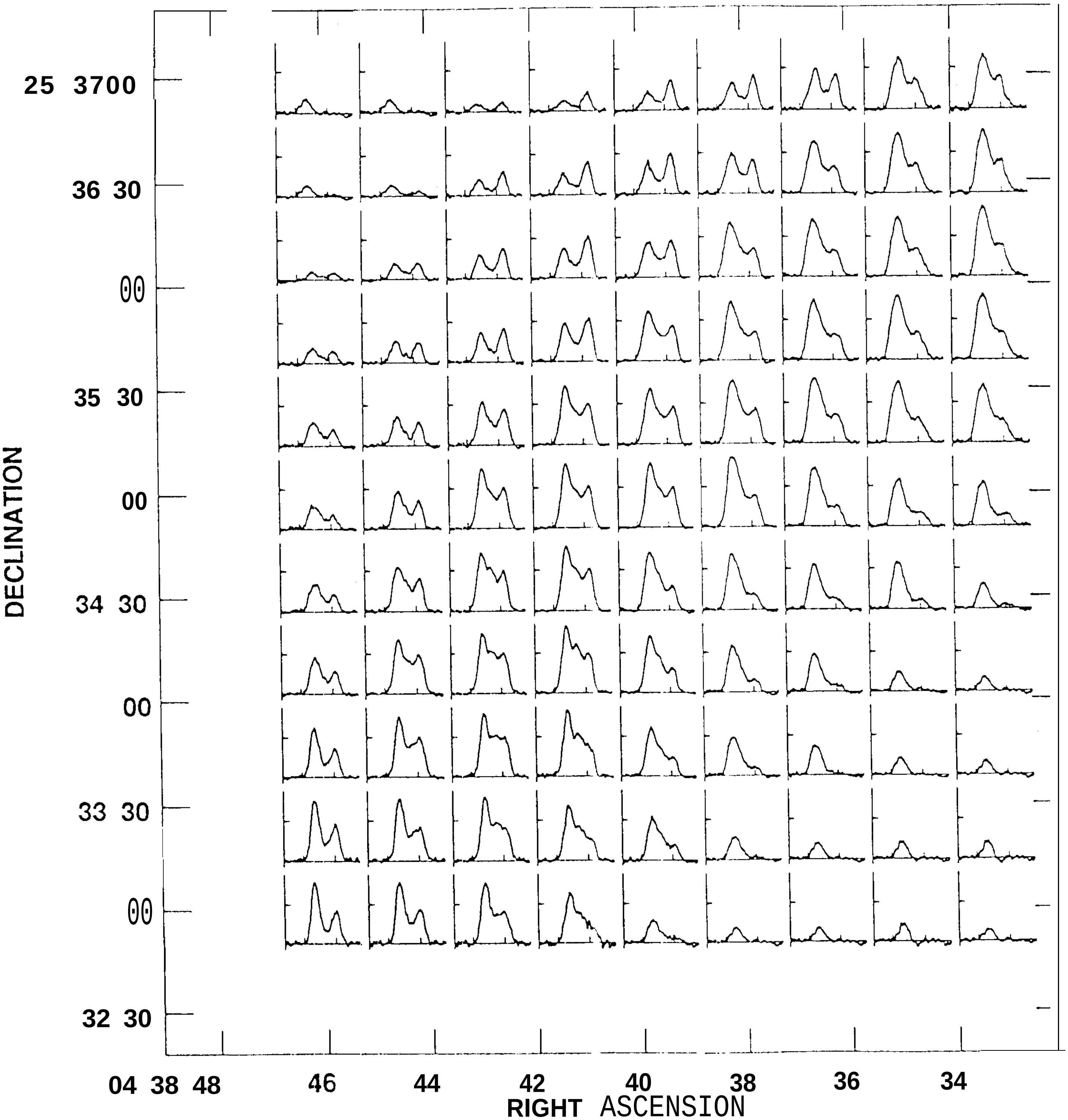
DECLINATION
25 3700
36 30
00
35 30
00
34 30
00
33 30
00
32 30
04 38 48
46
44
42
40
38
36
34
RIGHT ASCENSION

Fig. 3

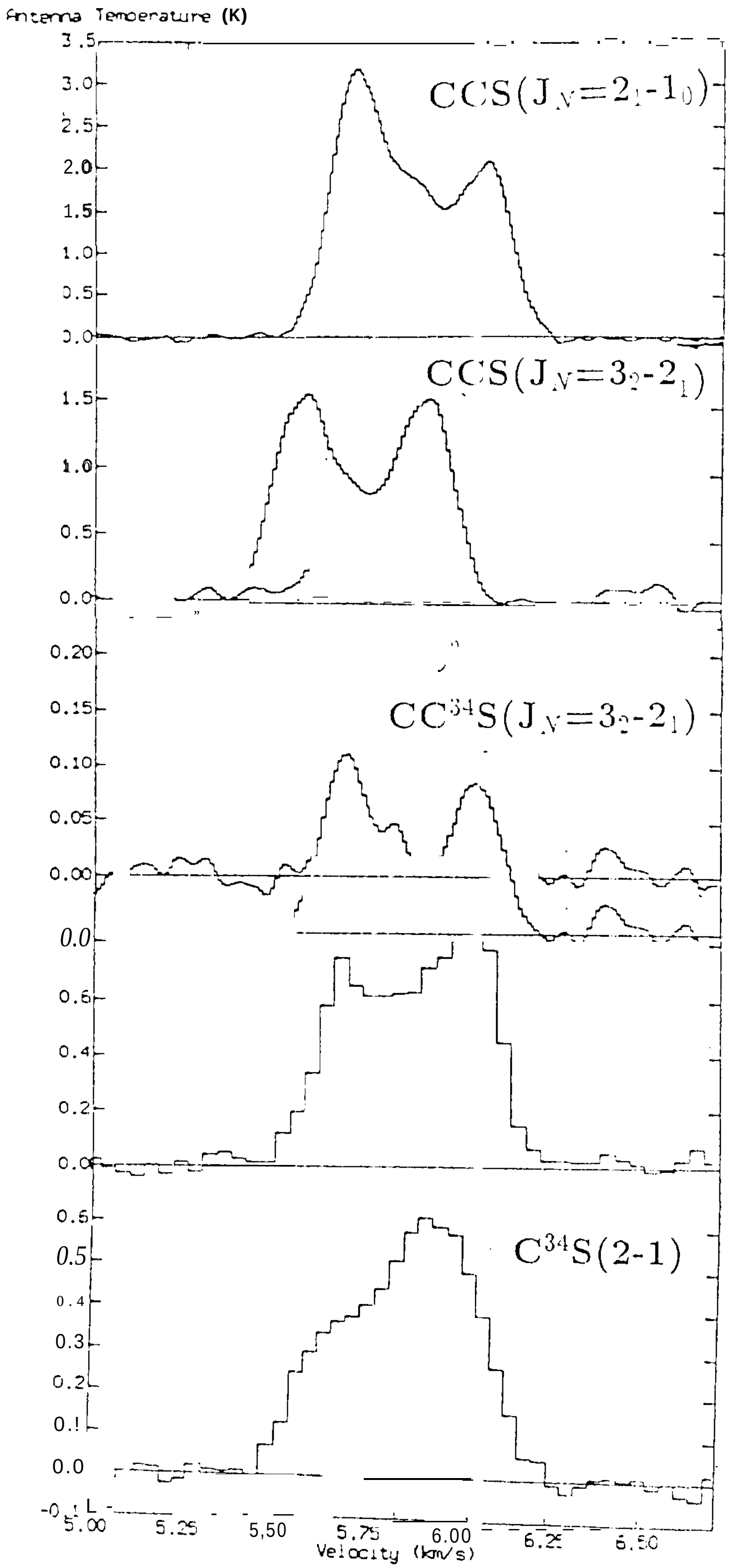

Antenna Temperature (K)
CCS(J_N=2_1-1_0)
CCS(J_N=3_2-2_1)
CC^{34}S(J_N=3_2-2_1)
C^{34}S(2-1)
Velocity (km/s)

Fig. 4

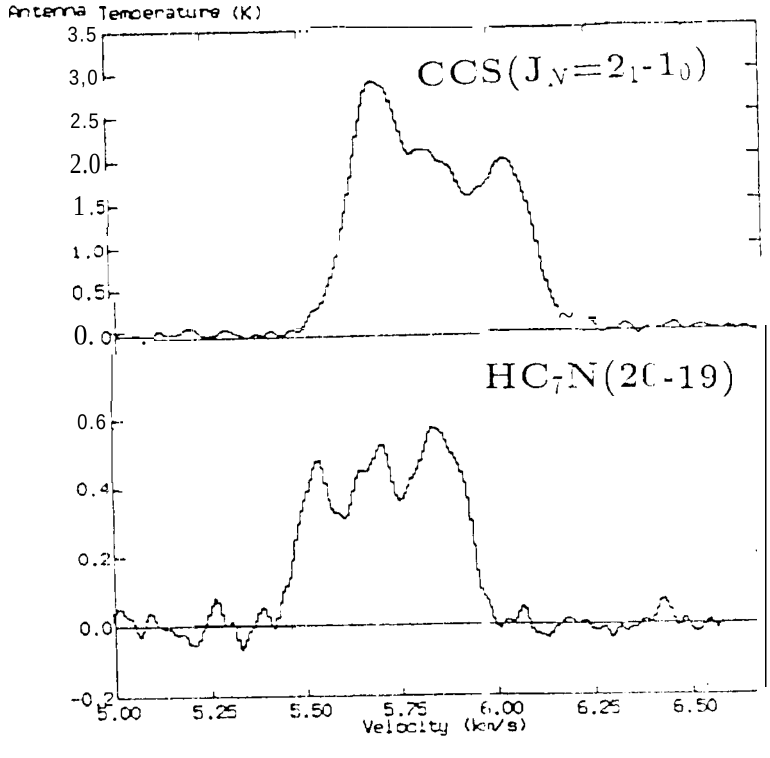

Fig. 5

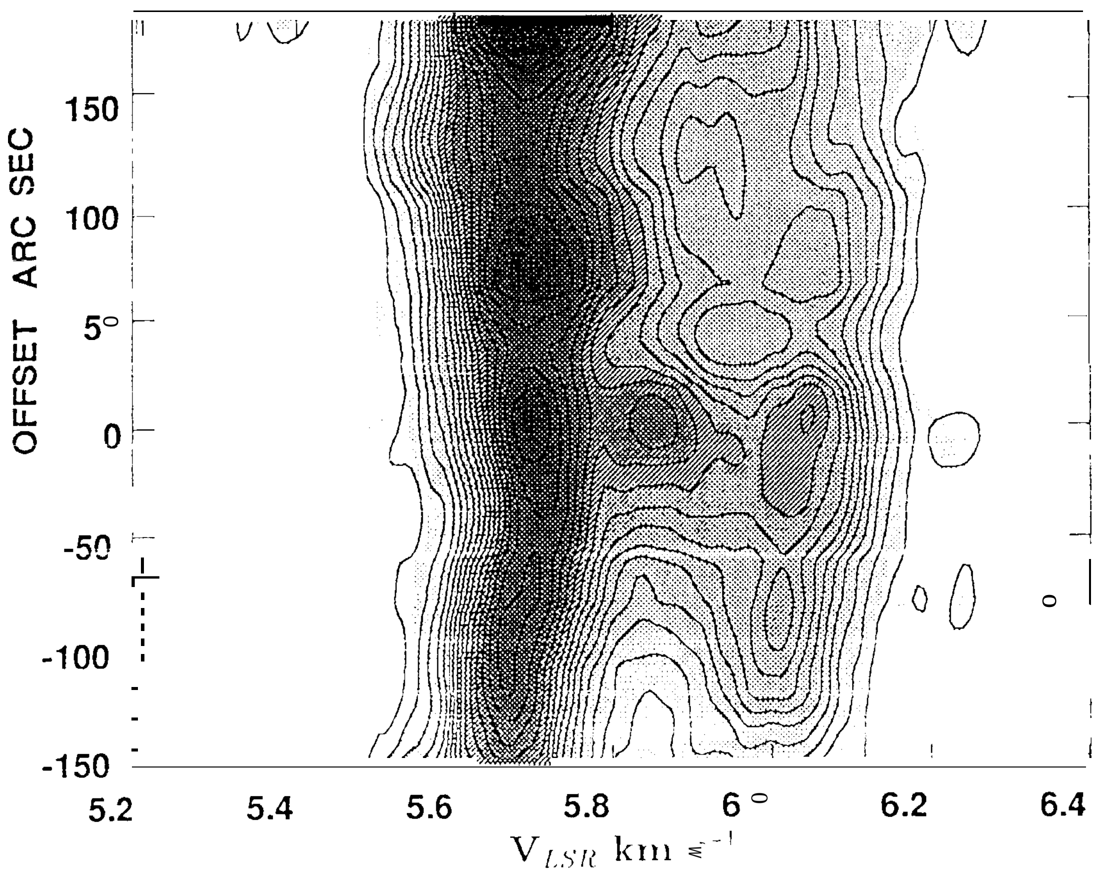
OFFSET ARC SEC
150
100
50
0
-50
-100
-150
5.2
5.4
5.6
5.8
6
6.2
6.4
V LSR km s-1

Fig. 6

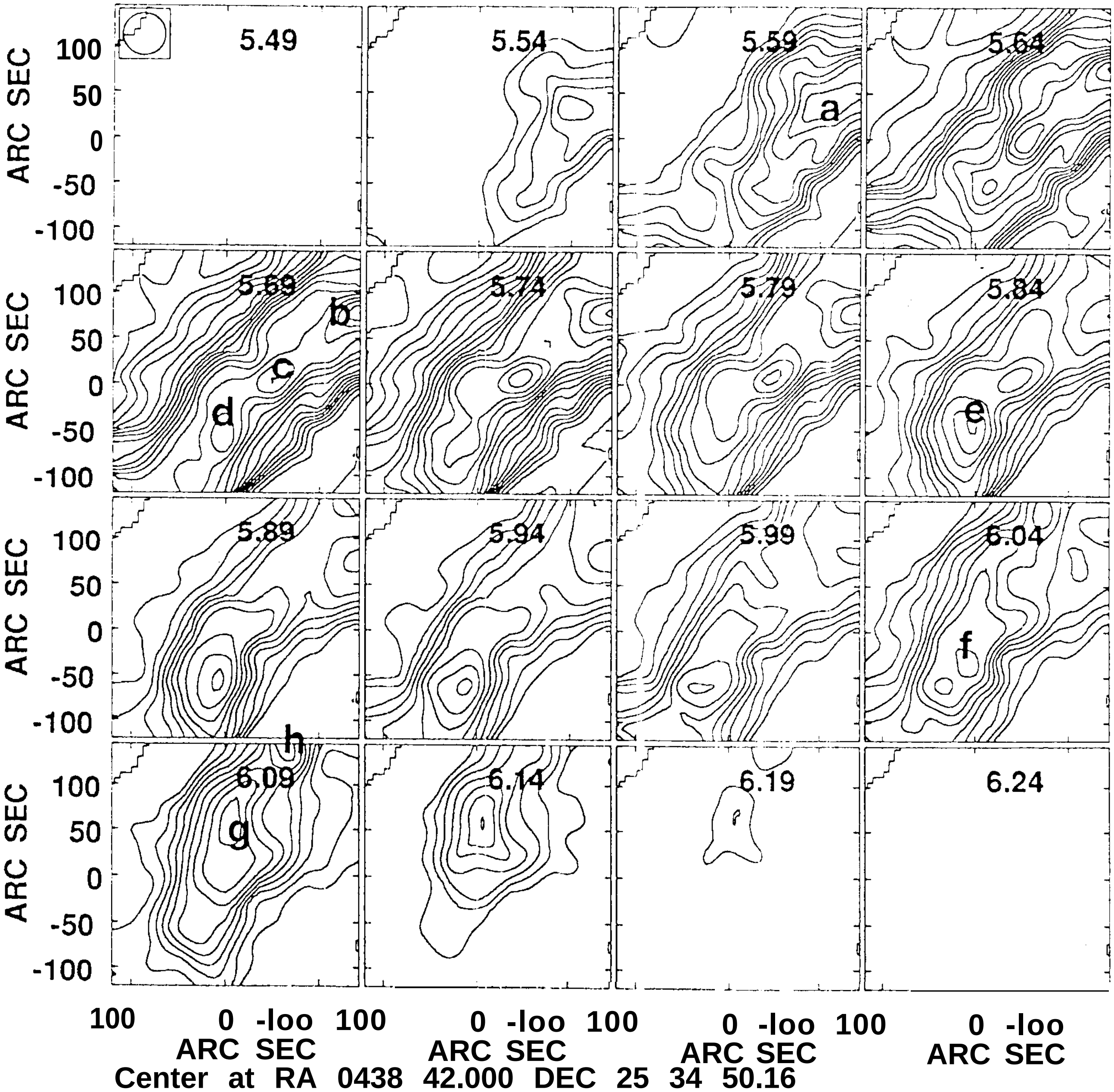
5.49
5.54
5.59
5.64
5.69
5.74
5.79
5.84
5.89
5.94
5.99
6.04
6.09
6.14
6.19
6.24
a
b
c
d
e
f
g
h
ARC SEC
100
50
0
-50
-100
100 0 -loo
ARC SEC
Center at RA 0438 42.000 DEC 25 34 50.16

Fig. 7

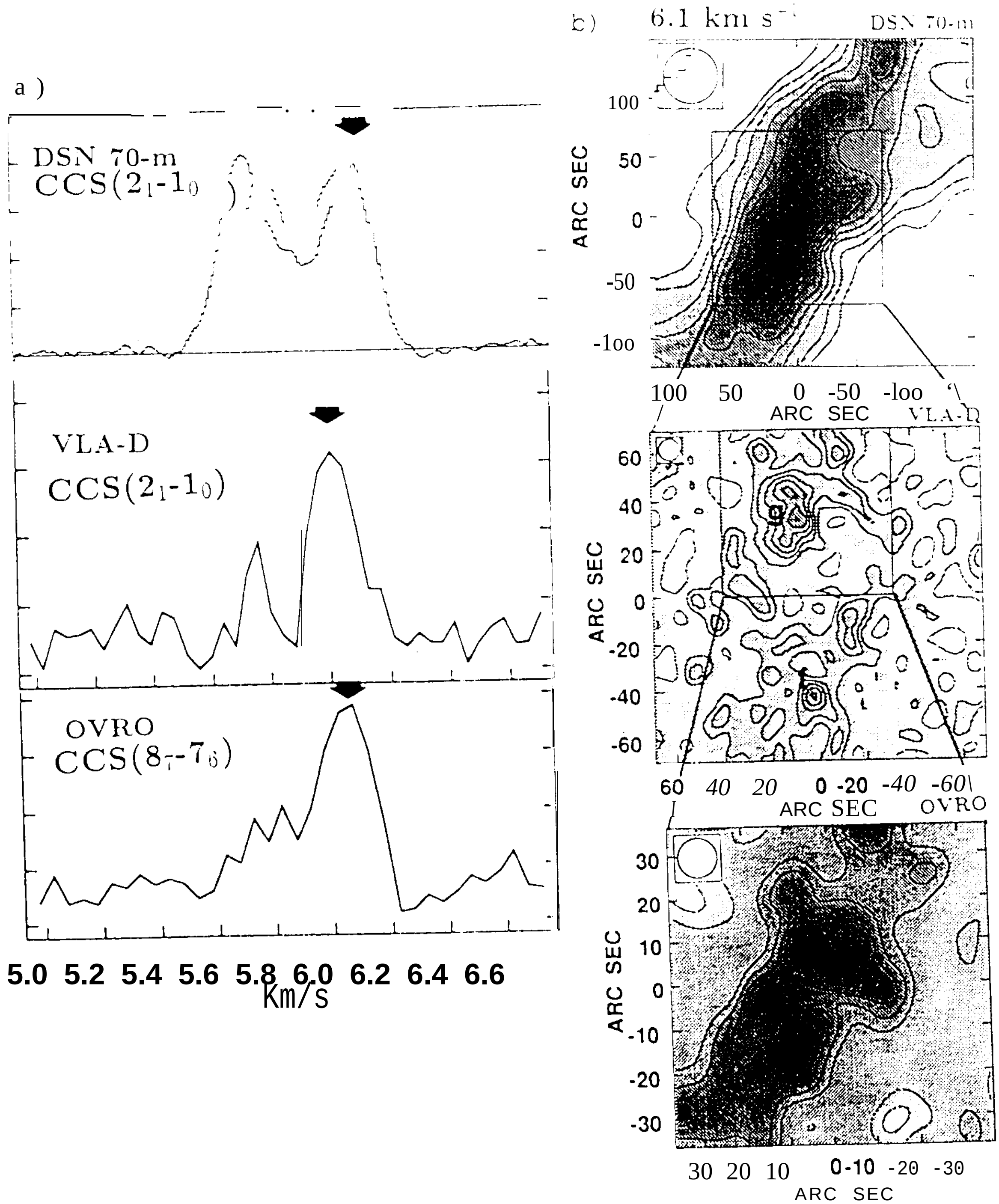

a)
DSN 70-m
CCS(2₁-1₀)
VLA-D
CCS(2₁-1₀)
OVRO
CCS(8₇-7₆)
5.0 5.2 5.4 5.6 5.8 6.0 6.2 6.4 6.6
Km/s
b)
6.1 km s⁻¹
DSN 70-m
100
50
0
-50
-100
ARC SEC
100 50 0 -50 -loo
ARC SEC
VLA-D
60
40
20
0
-20
-40
-60
ARC SEC
60 40 20 0 -20 -40 -60
ARC SEC
OVRO
30
20
10
0
-10
-20
-30
ARC SEC
30 20 10 0 -10 -20 -30
ARC SEC

Fig. 8

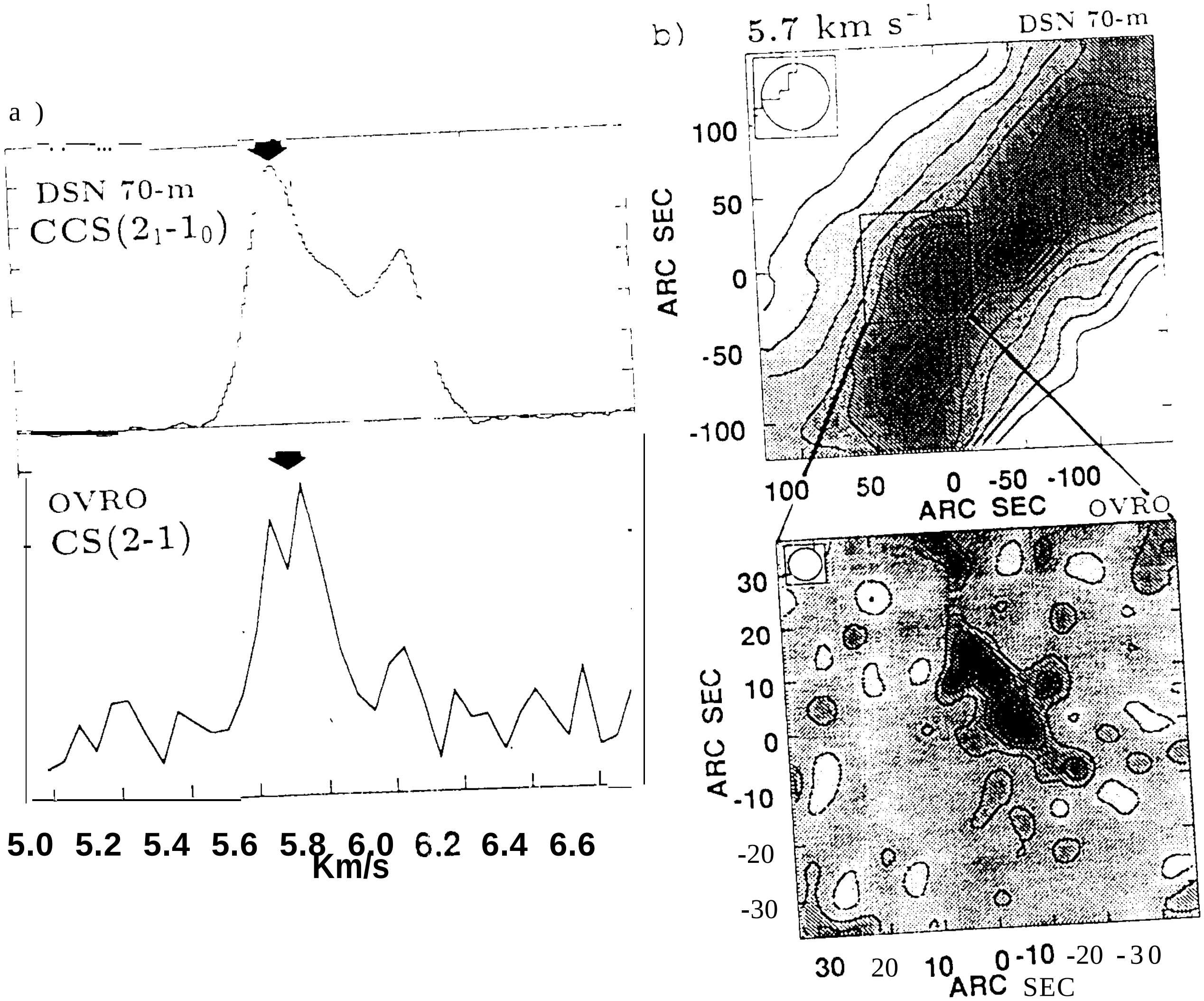
a)
DSN 70-m
CCS(2₁-1₀)
OVRO
CS(2-1)
5.0 5.2 5.4 5.6 5.8 6.0 6.2 6.4 6.6
Km/s
b)
5.7 km s⁻¹
DSN 70-m
ARC SEC
100
50
0
-50
-100
OVRO
30
20
10
-10
-20
-30

Fig. 9